HAL
open science

Analysis of High Energy Impact of a Raindrop on Water

Mohamed Houssein Ghandour, Annie-Claude Bayeul-Lainé, Olivier Coutier-Delgosha

To cite this version:

Mohamed Houssein Ghandour, Annie-Claude Bayeul-Lainé, Olivier Coutier-Delgosha. Analysis of High Energy Impact of a Raindrop on Water. Philippe Gourbesville; Guy Caignaert. Advances in Hydroinformatics. SimHydro 2019 - Models for Extreme Situations and Crisis Management, Springer Singapore, pp.907-922, 2020, 9789811554353. 10.1007/978-981-15-5436-0_69 . hal-03658522

HAL Id: hal-03658522

https://hal.science/hal-03658522v1

Submitted on 4 May 2022

HAL is a multi-disciplinary open access archive for the deposit and dissemination of scientific research documents, whether they are published or not. The documents may come from teaching and research institutions in France or abroad, or from public or private research centers.

L'archive ouverte pluridisciplinaire **HAL**, est destinée au dépôt et à la diffusion de documents scientifiques de niveau recherche, publiés ou non, émanant des établissements d'enseignement et de recherche français ou étrangers, des laboratoires publics ou privés.

ANALYSIS OF HIGH ENERGY IMPACT OF A RAINDROP ON WATER

[1]Mohamed Houssein Ghandour, [1]Annie-Claude.Bayeul-Lainé, [1, 2]Olivier Coutier-Delgosha

[1]Arts et Métiers ParisTech, LMFL, 8 bld Louis XIV, 59046 Lille cedex, France

[2]Virginia Tech, Aerospace & Ocean Engineering, 460 Old Turner street, Blacksburg 24060 VA, USA

Mohamed-Houssein.Ghandour@ensam.eu, Annie-Claude.Bayeul-Laine@ensam.eu, Olivier.Coutier-Delgosha@ensam.eu

KEY WORDS

Numerical simulation, drop impact, VOF, Transition model

ABSTRACT

The present paper is devoted to the analysis of the impact of a raindrop on water. The studied configuration is focused on the effects of high energy splash regimes, caused by the impact of large droplets at high velocity. Such cases, which mimic raindrops falling on the surface of the ocean at their terminal speed, are characterized by short time scales and complex mechanisms, and they have received little attention until now. The GERRIS opensource solver is used to perform three-dimensional simulations of the impact. The capabilities of octree adaptative mesh refinement enable to capture the small-scale features of the flow, while the Volume Of Fluid (VOF) approach combined with a balanced force surface tension calculation is applied to advect the volume fraction of liquid and reconstruct the interfaces. A post-processing of the results has been developed to identify each object resulting from the splash and characterize their evolution in time. Specifically, the contour of the liquid/gas structure created at the impact is reconstructed as well as the size and position of the ligaments and droplets aerosolized in the atmosphere. The results are compared to experimental data obtained previously by Murphy et al. (J. Fluid Mech., vol. 780, pp. 536–577): both the crown formation above the cavity created by the impact, the ligaments emanating from the rim at the top of the crown, and the downward liquid jet that pierces through the bottom of the cavity, are correctly reproduced by the model. A very good quantitative agreement is also obtained regarding the time evolution of the crown dimensions, including its closure after the initial phase of expansion.

1. INTRODUCTION

The impact of a droplet on a volume of liquid has been extensively studied since the initial work of Worthington (1882). In the specific case of identical liquids of density ρ, with a 90° impact of the droplet falling in air on a deep volume of target liquid, very different phenomena are still observed, when the liquid viscosity and surface tension σ with air, the diameter d of the droplet and the speed of the impact V are varied. Schotland (1960) has first reported the primary effect of the Weber number $\boldsymbol{We = \rho V^2 d/\sigma}$ on the physics of the impact, i.e. the ratio of the droplet kinetic energy to the energy required to deform the target liquid surface.

A few years later, Engel (1966) has provided a detailed description of the various behaviors obtained when We is varied in the range 50 – 150. Based on visualizations of the impact and using white particle in the target liquid and red ink in the droplet, he has shown that the drop impact creates a cavity in the flat free surface, and subsequently the rise of the target liquid in a cylindrical shape, from the edges of the cavity. A bubble-thin cylindrical sheet of liquid is erected at the upper edge of this crown, which eventually necks in and closes in a bubble dome in the most energetic test cases. After that, the cavity shallows and a jet forms at the cavity floor, which flows through the centre of the crown in case it's open or merges with a downward jet coming from the top of the bubble dome, in case the crown has closed. The author suggests that the cavity may vibrate at its maximal expansion, if all the drop kinetic energy is not yet transformed into potential energy, and he also assumes that (i) the maximum possible bubble height is equal to the cavity diameter, (ii) the pressure evolution below the cavity floor should explain the formation of the upward jet, (iii) the liquid of the initial drop is carried by this jet and will eventually form a secondary bubble at the centre of the cavity.

An exhaustive review of these previous works devoted to the impact of a droplet on a deep volume of the same low viscosity liquid has been conducted by Murphy et al. (2015), as can be seen in figure 1. Five different regimes have been identified by the authors, depending on the values of the Froude and Weber numbers. The two directions of variations of V and d are plotted in figure 1, as well as the specific case of raindrops of different sizes falling at terminal speed (solid black line labelled 'Raindrop TS').

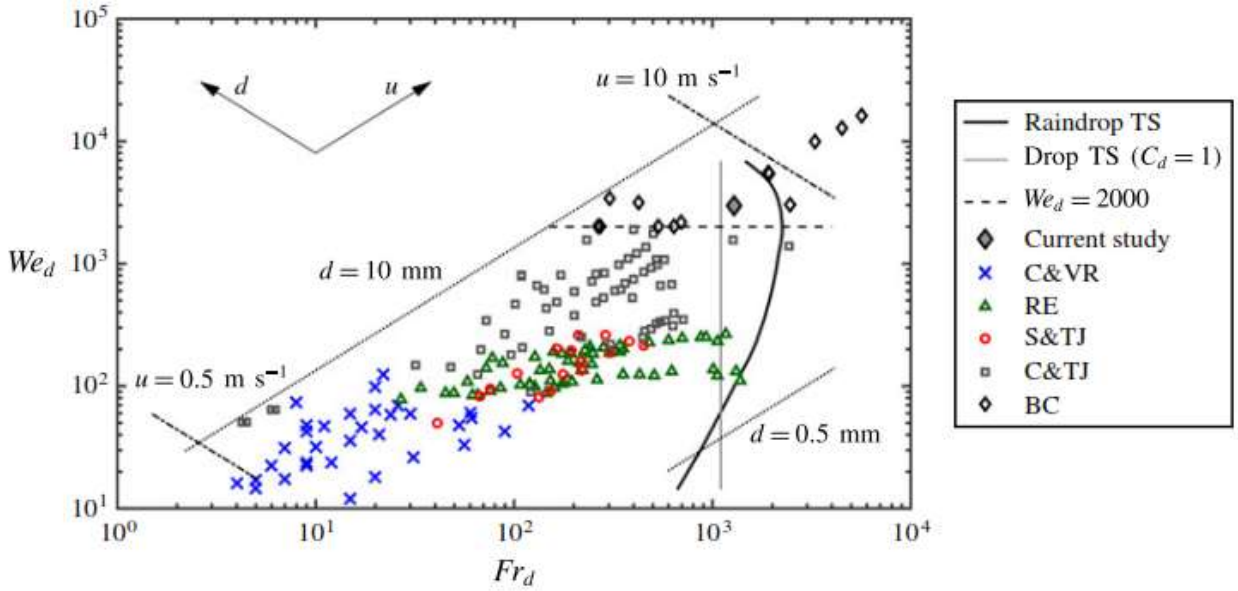

Figure 1. Various configurations of splashing reported in the literature according to the *We* and *Fr* numbers - reproduced from Murphy et al. (2015) with the authorization of the author.

As can be seen in the figure, if the droplet size and the impact speed increase (moving typically from the bottom left to the top right on the chart), the following successive regimes are obtained: (1) slow droplet that coalesces with the liquid volume and generates a vortex ring that moves downward as the droplet sinks, (2) formation of a cavity together with a surface wave, (3) the crater formed by the droplet increases and the surface wave forms a crown rim from which droplets and ligaments are ejected, (4) for the highest speeds and the largest raindrop diameters, a large cavity is obtained, around which extends vertically a very thin liquid film, whose elevation and radius increases before it eventually collapses in a very short time. At the upper part of the film, droplets and ligaments are ejected upward and outward.

This last type of behaviour (black diamonds in Figure 1) is the most energetic and it has been almost never studied until now (Bisighini et al. 2010). This high energy regime is characterized by shorter time scales and an increased complexity of the phenomena involved in the splashing, which makes both experimental and numerical approaches more challenging, and may explain why it has received less attention until now. However, it is the case likely to produce the greatest number of aerosol droplets. The present study is focused on this highly energetic case of large raindrops falling near terminal speed, which is representative of raindrops at the surface of the ocean.

This configuration has been studied by Murphy et al. (2015) in details, primarily as a reference case for a study focused on the influence of oil slicks and oil dispersant on the impact. High speed videos have enabled to characterize the time evolution of the external shape of the cavity, the crown and the upper rim, while microscopic holography has provided some statistics of droplet population ejected at the different stages of the process. These previous experiments are used to validate the numerical simulations conducted in the present study, which is focused on the same conditions of droplet diameter and speed at the impact. Further attention is given here to the internal mechanisms of crown and rim formation, as well as its violent closure, the liquid jets formed successively upward and downward and the subsequent entrainment of air bubbles, and the ejection of droplets at the edge of the upper rim, in various directions that depend on the stage of the process. Indeed, it was estimated in the experiments that such a large raindrop produces at least 2000 microdroplets. However, the details of the production of these droplets and statistics on their size, speed, and ejection direction remain to be found, which motivated the use of numerical simulations in this paper.

The numerical method is described hereafter in Section 2, and a comparison of our numerical results with experimental data is conducted in Section 3. The analysis of several mechanisms involved in the splashing is analysed in more details in section 4..

2. NUMERICAL SETUP

The Direct Numerical Simulations (DNS) consist in resolving all scales of the flow, from the smallest relevant ones (ideally here the smallest water droplets ejected in the air or air bubbles entrained in the water) up to the large scales of the problem (here the volume of sea water that receives the initial droplet impact). It means that the mesh of the water/air domain should be fine enough to capture all air/water interfaces created at all steps of the splashing process.

2.1 Main features of the solver

GERRIS is a flow solver developed by (Popinet, 2003) and available for use and development under a free software GPL license. It solves the time-dependent incompressible variable-density Euler, Stokes, or Navier-Stokes equations with second order space and time accuracy. To calculate liquid / gas flows, it solves a system of equations (1) to (3), i.e. the 3 momentum balance equations, the mass balance equation, and the advection of the volumic proportion of gas $\beta(\vec{X},t)$, called hereafter the void fraction.

$$\rho\left(\frac{\partial\vec{U}}{\partial t}+(\vec{U}\cdot\vec{\nabla})\vec{U}\right)=-\vec{\nabla}P+\vec{\nabla}\cdot(2\mu\overline{\overline{D}})+(\rho-\rho_g)\vec{g}+\sigma\kappa\delta_s\vec{n} \tag{1}$$

$$\vec{\nabla}\cdot\vec{U}=0 \tag{2}$$

$$\frac{\partial\beta}{\partial t}+\vec{\nabla}\cdot(\beta\vec{U})=0 \tag{3}$$

Where $\vec{U}(\vec{X},t)$ is the velocity, $\rho(\vec{X},t)$ is the density, ρ_g is the air density, $\vec{X}$ is the position, P is the pressure, $\mu(\vec{X},t)$ is the viscosity, $\overline{\overline{D}}$ is the deformation tensor, which components are $D_{ij}=\partial u_i/\partial x_j+\partial u_j/\partial x_i$ with u_i and x_i, i=1 to 3 the components of $\vec{U}$ and $\vec{X}$, respectively. The last term in equation (1) is the surface tension force, with κ the curvature of the interface, σ the surface tension coefficient, and $\vec{n}$ the unit vector normal to the interface. This term is zero everywhere but at the liquid/gas interface, as controlled by the Dirac function δ_s.

The density and viscosity are calculated according to the following relations:

$$\rho=\beta\rho_g+(1-\beta)\rho_l \tag{4}$$

$$\mu=\beta\mu_g+(1-\beta)\mu_l \tag{5}$$

Where ρ_g, ρ_l are the air and water densities, and μ_g, μ_l are the air and water viscosities.

A time splitting projection method is used to discretize the equations (1) to (3), leading to the following expressions:

$$\rho^{n+1/2}\left(\frac{\vec{U}^*-\vec{U}^n}{\Delta t}+\left(\vec{U}^{n+1/2}\cdot\vec{\nabla}\right)\vec{U}^{n+1/2}\right)=\vec{\nabla}\cdot\left(\mu^{n+1/2}\left(\overline{\overline{D}}^*+\overline{\overline{D}}^n\right)\right)+(\sigma\kappa\delta_s\vec{n}-\rho\vec{g})^{n+1} \tag{6}$$

$$\vec{U}^{n+1}=\vec{U}^*-\Delta t\left(\frac{\vec{\nabla}P}{\rho}\right)^{n+1/2} \tag{7}$$

$$\vec{\nabla}\cdot\vec{U}^{n+1}=0 \tag{8}$$

$$\frac{\beta^{n+1/2}-\beta^{n-1/2}}{\Delta t}+\vec{\nabla}\cdot(\beta\vec{U})^n=0 \tag{9}$$

The following steps are performed to solve the equations:

1) The estimate velocity field $\vec{U}^*$ is computed from equation (6), using a variant of the multilevel iterative Poisson solver described in detail in Popinet (2003), and a collocated grid discretization (all variables are computed at the center of the cells).

2) The estimate velocity is interpolated at the center of the faces and used to compute $\vec{\nabla} \cdot \vec{U}^*$ according to the following equation:

$$\vec{\nabla} \cdot \vec{U}^* = \frac{1}{L} \sum_{faces} \vec{U}_k^* \cdot \vec{n}_k \tag{10}$$

Where $\vec{n}_k$ is the unit vector normal to face k, $\vec{U}_k^*$ is the estimate velocity at the center of face k and L is the dimension of the cell. This calculation enables to avoid spurious pressure oscillations that would result from the resolution of the pressure equation at next step with all variables taken at the center of the cells.

3) Equations (7) and (8) are combined to build the following pressure equation:

$$\Delta t \ \nabla \cdot \left(\frac{\nabla P}{\rho}\right)^{n+1/2} = \vec{\nabla} \cdot \vec{U}^* \tag{11}$$

Which is solved using a quad/octree based multigrid iterative Poisson solver described in detail in Popinet (2003) and shown to be second-order accurate. Then, face velocities $\vec{U}_k^{n+1}$ are corrected according to equation (7) using a face centered pressure gradient and interpolated values of β at the center of the faces to calculate $\rho^{n+1/2}$. The cell-centered velocities are also recalculated with equation (7), using interpolated values of the face-centered pressure gradients. The resulting face-centered and cell-centered velocity fields are exactly and approximately divergence free, respectively.

4) Equation (9) is solved using a piecewise-linear geometrical VOF scheme initially proposed by Scardovelli & Zaleski (2000) and later generalized for the octree spatial discretization (Popinet 2009). The method of interface normal computation with a 3×3×3 compact stencil developed by Aulisa et al. (2007) for regular cartesian grids is extended to variable spatial resolution along the interface (Popinet 2009). The volume fraction is advected using an operator-split algorithm initially implemented by DeBar (1974), using a volume flux computed from the geometry of the reconstructed interface (see Popinet 2009 for the generalization to the octree discretization).

5) The surface tension force $(\sigma\kappa\delta_s\vec{n})^{n+1/2}$ is calculated with the balanced-force surface-tension calculation used by Francois et al. (2006), which is based on the Continuum-Surface-Force (CSF) approach originally proposed by Brackbill (1992):

$$\sigma\kappa\delta_s\vec{n} \approx \sigma\kappa\vec{\nabla}\tilde{\beta} \tag{12}$$

where $\tilde{\beta}$ is the spatially averaged void fraction.

2.2. Flow configuration and adaptive mesh refinement

The configuration of droplet impact investigated in the present study mimics the one studied by Murphy et al. (2015), using high speed video. In the experiments, the droplet falls in a 15.2 × 15.2 cm^2 tank filled with seawater to a depth of 8 cm. The measured horizontal and vertical diameters of the droplet just before the impact are $d_h =$ 3.8 mm and $d_v =$ 4.2 mm, respectively, which results in an average diameter $d \approx 4$ mm. The speed before impact is 7.2 m/s, which is 81% of the drop terminal speed.

In the present simulations, the computational domain is reduced down to a cube of dimensions 6.4 × 6.4 × 6.4 cm^3, which represents about 1/8 of the water tank volume in the experiments. It has been found to be the best compromise to avoid any effect of the boundary conditions on the splashing, while decreasing as much as possible the dimensions of the domain. The free surface is located at mid-distance between the bottom and the top, to give enough space to the aerosolized droplets without any interaction with the top boundary condition.

The water in the droplet and in the tank are the same, which is assumed to have almost no effect on the splashing, as the properties of the fresh water drop and the target seawater in the experiments are very close.

Cubic finite volumes organized hierarchically in octree are used for space discretization. The octree structure has been developed initially for image processing (Samet, 1989) and later applied to CFD (Khokhlov 1998) and multiphase flows (Popinet 2003). The basic organization is the following, all details can be found in (Popinet 2003): when a cell is refined, it is divided into 8 cubic cells, whose edges are half the ones of the parent cell. The base of the tree is the root cell and the last cells with no child are the leaf cells. The cell level is the number of times it is refined, compared with the root cell (level 0). To avoid too much complexity in the gradient and flux calculations, the levels of direct and diagonally neighboring cells are constrained and cannot differ by more than one.

As a parallel computation with 2048 processors was conducted to simulate the drop impact, the initial mesh is composed of 20^3 = 8,000 blocks to ensure a good balance of the processor loadings. Indeed, each root block cannot be shared by two processors, so the number of initial cells should be significantly larger than the number of processors, to guarantee that each of them will be in charge of in charge of a significant number of interfaces. The maximum number of refinements was set to n_{max} = 6 for a preliminary calculation and n_{max} = 8 for the final simulation analyzed in this paper. The resulting smallest resolved scales are 50 µm and 12.5 µm, respectively. Note that the more the maximum refinement level is increased, the more the time steps are reduced to comply with the CFL (Courant–Friedrichs–Lewy) condition, which means that the calculation CPU time is not proportional to the number of cells: it has been estimated that each additional levels scales the computational cost by a factor 3 to 5. The initial mesh is refined at the free surface and the boundary of the drop at level 5, as can be seen in figure 2.

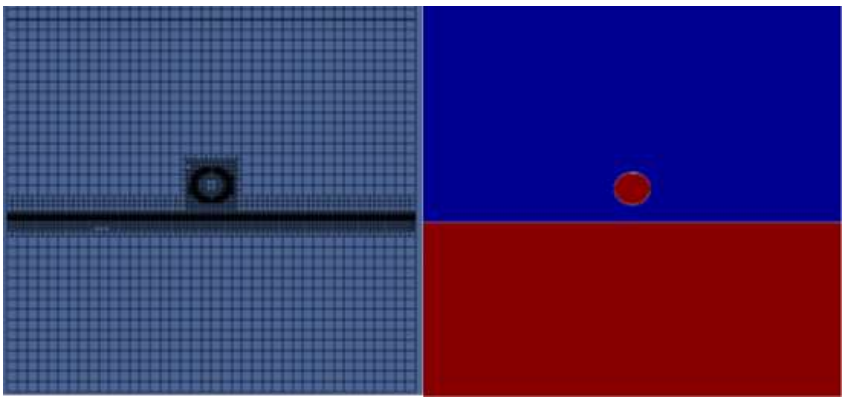

Figure 2. Initial flow configuration (water in red, air in blue) and related local refinement

The mesh refinement is performed every time step using appropriate criteria like vorticity, gradient of a field variable or the curvature of the interface. In the present calculation, the simplest is to refine according to the void fraction: any cell where $0 < \beta < 1$ is refined as much as allowed, in the limits of the constraints mentioned above. However, the number of interfaces increases drastically after a few milliseconds, as soon as the impact generates complex structures like the crown, the ligaments at the edge, and multiple aerosols. To reduce the computation time, several strategies of mesh refinement have been tested:

(a) Default criterium based on the local void fraction: $0 < \beta < 1$

(b) Criterium based on the gradient of the void fraction scaled by the local velocity: $\|\vec{\nabla}((1-\beta)\ V)\| > C_1$: the objective is to exclude all areas where the velocity is very small, assuming that a precise definition of the interface is not needed. It concerns mostly the free surface far from the impact, where nothing happens during a significant part of the simulation. C_1 is a constant equal to 10^{-3} for 0 < t < 2 ms, and 10^{-4} for t > 2 ms. Indeed, the order of magnitude of the velocities is much higher at the beginning of the process than after the impact, so the condition must be adjusted.

(c) Combination of two criteria: $\|\nabla(1-\beta)\| > C_2$ and $\nabla \cdot U > C_3$, which is another way to take into account the local dynamics.

(d) Combination of $0 < \beta < 1$ and $\vec{\nabla} \cdot \vec{U} > C_3$

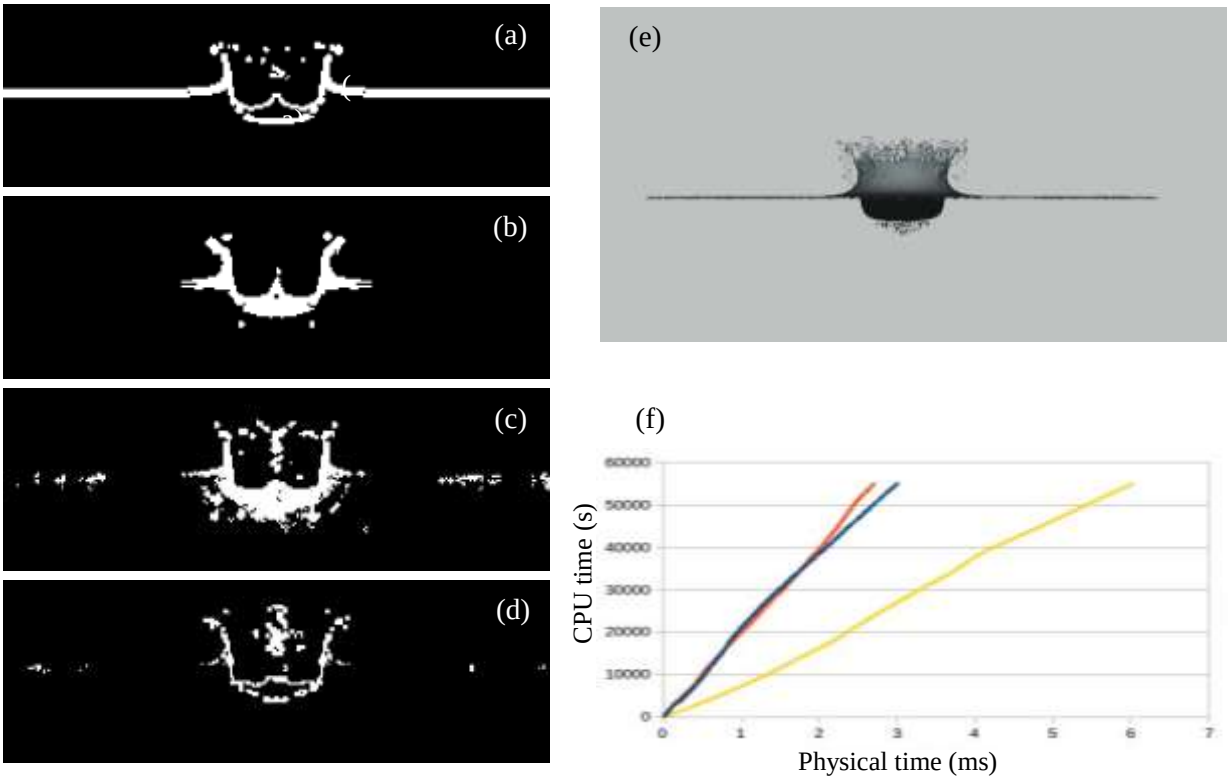

Figure 3: Optimization of the mesh refinement process, with criteria based on: (a) $0 < \beta < 1$, (b) $\|\vec{\nabla}((1-\beta)\ V)\| > C_1$, (c) $\|\vec{\nabla}(1-\beta)\| > C_2$ and $\vec{\nabla} \cdot \vec{U} > C_3$, (d) $0 < \beta < 1$ and $\vec{\nabla} \cdot \vec{U} > C_3$. Figure 3e shows the aspect of the splashing at the same time, and figure 3f displays the CPU time in cases (a) red, (b) blue and (d) yellow from t = 0 to 6 ms.

Figure 3 displays the areas of leaf cells at time t = 1 ms, i.e. right after the impact, when the cavity has started to develop, the ejected water at the periphery of the impact is rising and form the crown, and the water coming from the droplet is at the bottom at the crater. These results were obtained with $n_{max} = 6$ for the purpose of preliminary tests, so their accuracy is not discussed here. Figure 3 shows that option (b) does remove the useless refinement of the free surface, but it also induces additional fine cells in all liquid areas with non-zero velocities, like within the volume of droplet water at the floor of the cavity. As the primary objective is to focus the mesh refinement on the interfaces only, this is not satisfactory. Option (c), although it simplifies the tuning of the constants by separating the effect of the velocity and the void fraction, does not improve the previous issue. The best result was eventually obtained with option (d), which is applied in the simulations presented hereafter.

A first simulation ($n_{max} = 6$) was run with 64 processors available at University of Lille. The second simulation ($n_{max} = 8$) was run partially with the same computational ressources, and eventually on the ADA machine of the IDRIS French National facility, using 2048 processors.

2.3. Post-processing

The GERRIS solver provides, at each time step where the solution is stored, the field of void fraction β. For the purpose of comparison with the experiments and analysis of the splashing, it is necessary to extract from this information quantitative data about the cavity and crown evolutions, as well as the population of aerosolized droplets. Therefore, each individual object having an interface should be characterized, which requires to reconstruct the liquid / gas interfaces and identify all these objects.

A post-processing has thus been developed. The basic idea is to mark all cells that have a void fraction $0 < \beta < 1$, then to start from one of them loop into all contiguous cells to check which ones are part of the same interface. Successive iterations enable to find all cells belonging to one object, then this object can be removed, and the process is restarted until all objects have been reconstructed. However, this process is very time consuming in three dimensions, and the octree structure makes it significantly more complicated, as some interfaces may be defined on different levels of refinement. Therefore, the following algorithm is eventually applied:

1) All n_{cells} cells where $0 < \beta < 1$ are identified and given an ID number. It includes cells at all levels of refinement, from n_{min} (minimum refinement level present in the domain) up to n_{max}. The cells are sorted in a specific order based on the components (x, y, z) of their center. M_{cells} is the $3 \times n_{cells}$ matrix that contains the x, y and z positions of all cells, for $0 < ID < n_{cells}$. For each level of refinement n, a matrix M_{cells}^{n} containing the cells at level n is extracted from M_{cells}. The next steps of the process consist of a loop from n_{min} to $n_{max} - 1$, which enables to manipulate not all the cells at the same time, and also to detect progressively some interfaces that may be defined at different levels.

2) For $n = n_1 = n_{min}$, cells of $M_{cells}^{n_{min}}$ and $M_{cells}^{n_{min}+1}$ are considered. For each cell C_{ID}, 3 blocks oriented in the x, y, and z direction, respectively, are created. The x-oriented block is based on the stencil of 10 cells composed of C_{ID} and the 9 cells surrounding C_{ID} in the y and z directions: that stencil is extruded in the x direction to the ends of the domain (see figure 4 in two dimensions, extension to three dimensions is straightforward). All cells included in the x-oriented block associated to cell C_{ID} are identified in the vector M_x^{ID}, through a Boolean information: each component $m_{x\ i}^{ID}$ is TRUE or FALSE, depending if the cell whose ID equals i is part of the block. Two other vectors M_y^{ID} and M_z^{ID} are built with the y-oriented and z-oriented blocks. The term by term multiplication of vectors M_x^{ID}, M_y^{ID} and M_z^{ID} provides the IDs of all cells contiguous to C_{ID}.

3) Step 2 is initiated with a first cell C_{ID} belonging typically to the free surface / cavity / crown structure, which is the biggest object to be detected. All detected contiguous cells are marked, and the same process is repeated for all cells of $M_{cells}^{n_{min}}$ and $M_{cells}^{n_{min}+1}$, which enables to detect and mark all cells of level n_{min} that belong to the structure, and most of the cells at level n_{min}+1 (see step 4 hereafter). Figure 5 shows an example of the process: eventually all blue dots (centers of cell at level n_{min} and most of the orange dots (centers of cells at level n_{min}+1) will be detected. Note that this method of detection is very fast, as step 2 is based on a single term by term vector multiplication to detect up to 27 contiguous cells.

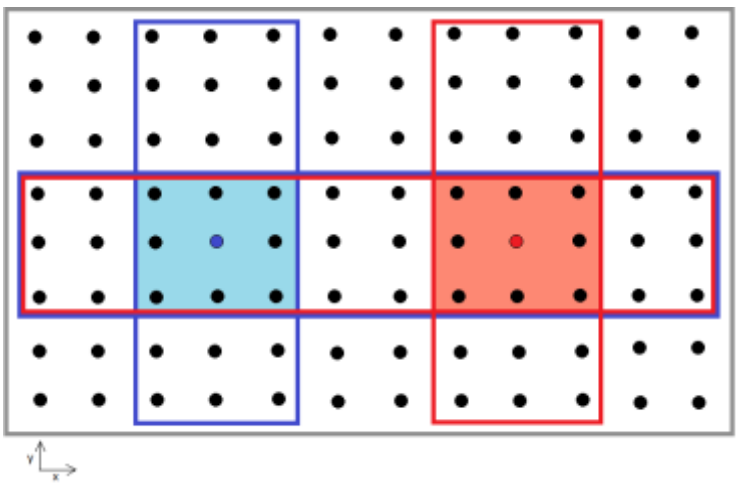

Figure 4: Scheme of of the x and y-oriented blocks in two dimensions for the cells colored in blue and in red, respectively. The blocks are the rectangles of the same colors, extended to ends of the domain (in grey) in the x or y direction. Once the vectors containing the Boolean information of the cell presence in the blocks are multiplied term by term, the cells in the shaded areas are identified.

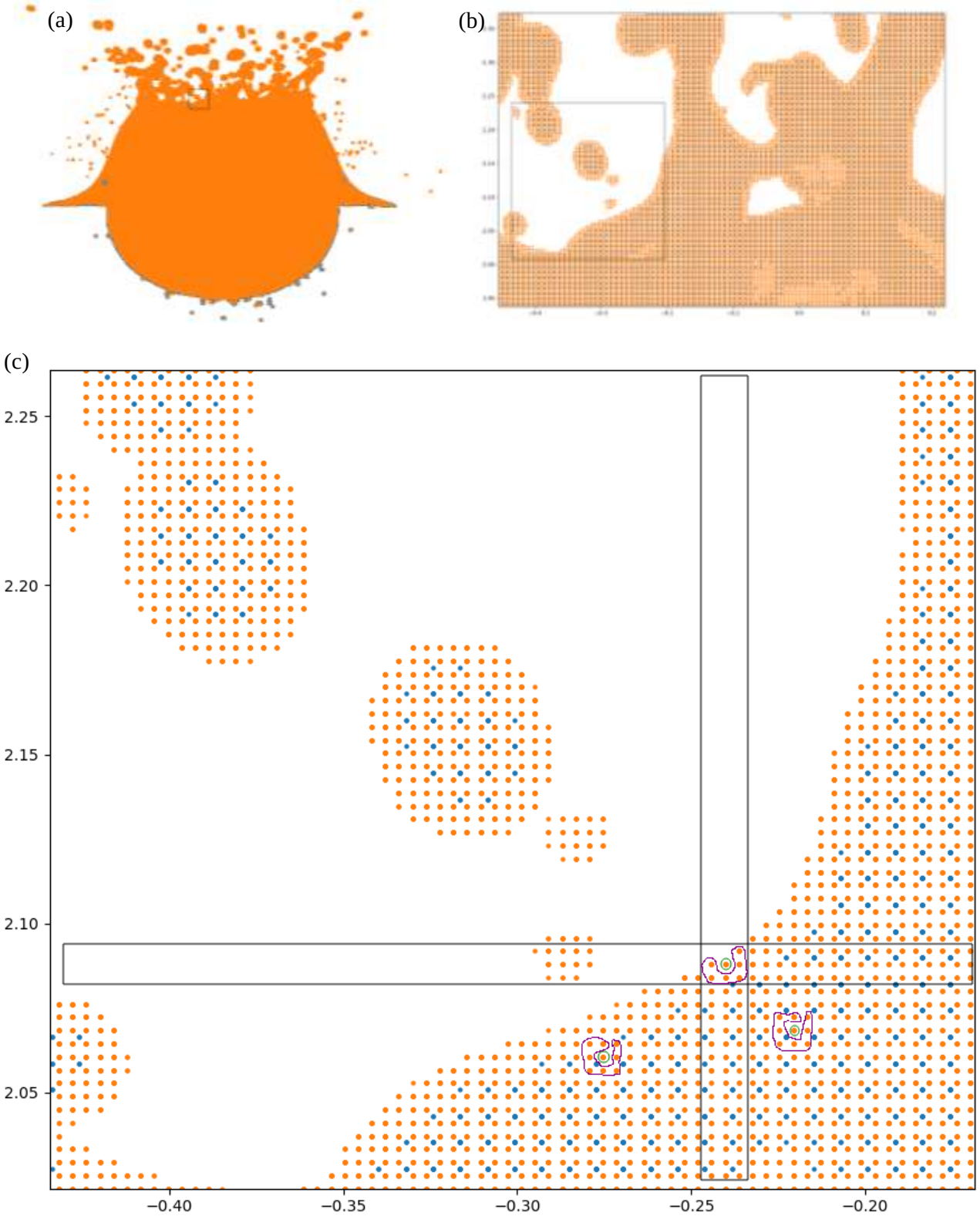

Figure 5: Two-dimensional example of object identification in the area shown in pictures (a) and (b). Using the x, y and z-oriented blocks (see picture 5c), cell detection is performed at levels k (blue dots) and k+1 (orange dots), starting from one of the dots circled in green. Dots circled in violet are eventually detected. This process is repeated, starting successively from all detected cells, until all contiguous cells velonging to the object are detected. In this example, 6 objects would be detected : the crown (at the bottom of the picture) and 5 droplets. Note that at the previous step (using cells at levels k-1 and k-2), three droplets only could be detected, as three droplets have cells at level k only, and an other one was falsely split into two different objects at level k-1.

4) Steps 2 and 3 are repeated for a higher level of refinement $n_2 = n_{min} + 1$, using cells of $M_{cells}^{n_{min}+1}$ and $M_{cells}^{n_{min}+2}$. Additional cells at level $n_{min} + 1$ may be found, in case they are connected to the object via cells at level $n_2 + 1 = n_{min} + 2$, like in the case of the droplet at the top left of figure 5c: the detection of contiguous orange cells enables to find the complete drop, while the blue cells are not all contiguous so all blue cells were not detected at the previous step. This process is repeated for all higher levels up to $n_{max} - 1$, where all cells at level n_{max} are eventually detected and marked.

5) At the end of step 4, the main object is completely detected, and all marked cells are removed from the vectors M_{cells}^{i}, $n_{min} < i < n_{max}$. Then, steps 2 to 4 are repeated, starting from one of the undetected cells at level n_{min}, until all other objects (i.e. the aerosolized droplets) are also found.

3. RESULTS AND DISCUSSION

The numerical results obtained with n_{max} = 8 are compared hereafter to the experimental data. This value of n_{max} was selected after the first calculation (n_{max} = 6) has revealed some significant discrepancies with the experiments (see figure 6): it can be observed that the general shape of the crown is not consistent with the experimental visualizations, the height is too small and the radial extension too large. In addition, the ligaments are not correctly oriented.

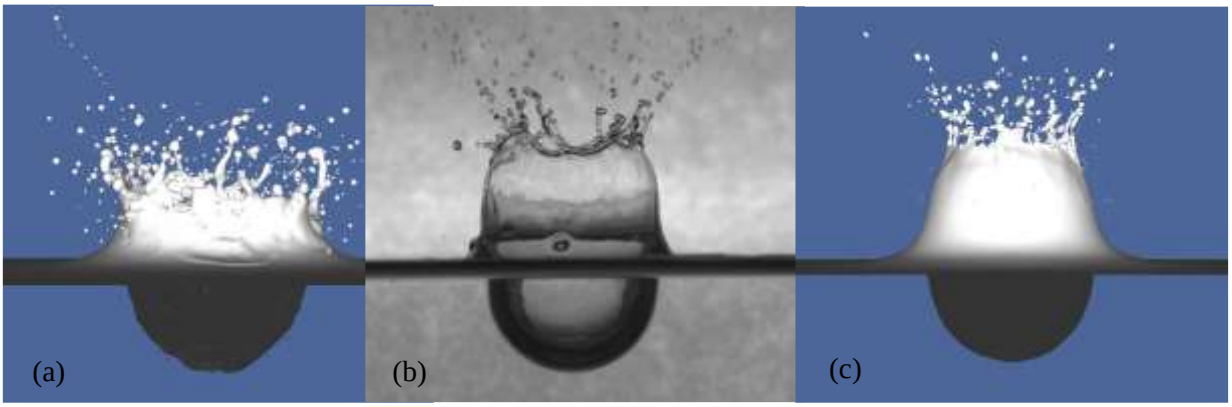

Figure 6: Shape of the cavity and the crown at t = 7 ms. (a) calculation with n_{max} = 6, (b) experiments, (c) calculation with n_{max} = 8. The scale is the same on all pictures.

As a formal study of time step and mesh influence could not be performed, given the computational time required for the simulations, a detailed qualitative and quantitative comparison with the data reported in murphy et al. (2015) is conducted, which will eventually validate the present numerical strategy, and therefore enable the discussion of the splashing mechanisms in a future work.

Figure 7 shows the global evolution of the observable events in the experiments, during the 85 ms that were simulated. It can be seen that the computation reproduces all the features of the splashing, namely the flat bottom cavity at the early stage of the crater development (t = 1 ms), the growth of the upper rim with the ligaments oriented outwards at the top edges (t = 3 ms), the ejection of the droplets at the end of the ligaments (t = 8 ms), the closure of the upper rim (t = 17 ms), which results in a downward liquid jet that pierces the cavity bottom at t = 43 ms and finally a broad upward jet at t = 85 ms. The correct prediction of the rim height, the angle of the ligaments, and the exact time where the downward jet pierces the cavity floor is especially convincing.

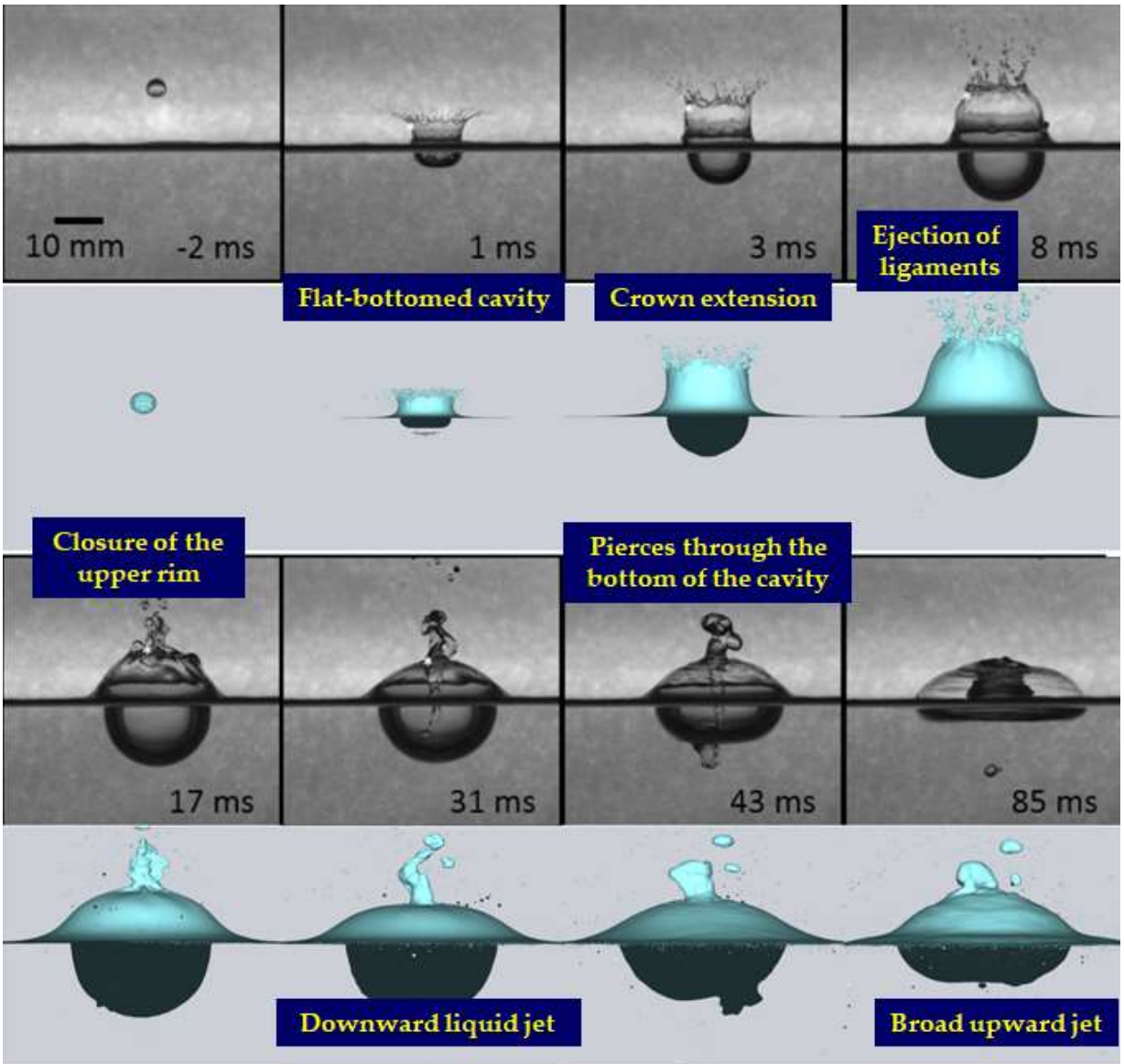

Figure 7: Comparison between experiments and simulation during 85 ms after the impact. Top picture are extracted from high speed imaging (Murphy et al. 2015), bottom pictures are the present simulations.

Quantitative comparisons are displayed hereafter: to characterize the time evolution of the upper rim, its radius and height are calculated at all times from the crown formation to its closure. The height is defined as the distance between the initial free surface and the position where the ligaments are forming. In practice, that position is determined according to the numbers of cells included in the crown between the top and a given altitude: this number decreases linearly as z is increased from 0 to the basis of the ligaments, then the slope suddenly changes (see figure 8) above this limit. Therefore, the position of this change of slope was used to define the height and the radius of the crown, which are displayed in figure 9.

A reliable agreement is obtained between the simulations and the experiments, from the crown formation (first millisecond) to the closure of the upper rim (t = 10 to 15 ms). Figure 10 confirms this conclusion: both the cavity volume evolution (during the entire simulation) and the trajectory of the edges of the upper rim are also found in very good agreement with the experimental measurements.

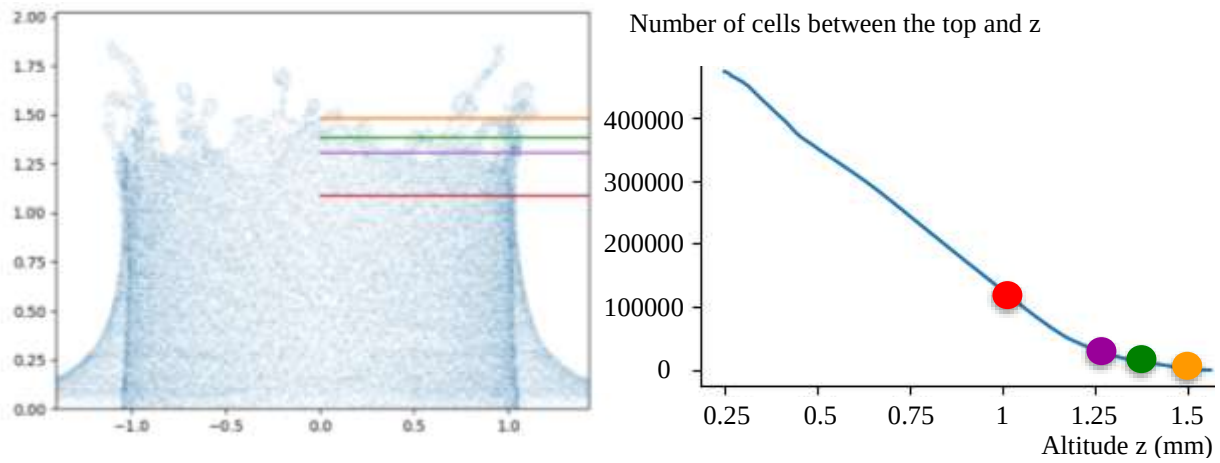

Figure 8: definition of the position where the rim radius and height are calculated (violet point / line)

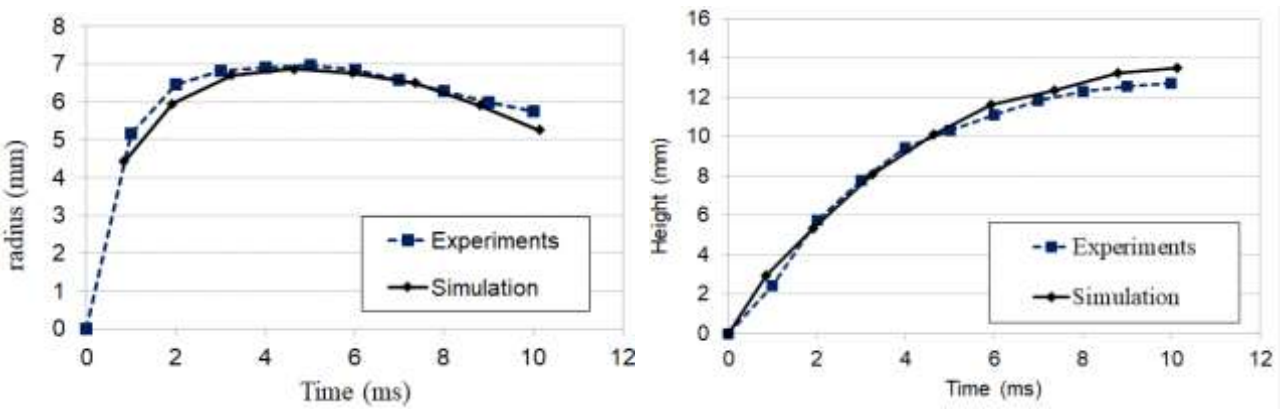

Figure 9: evolution of the crown radius and height

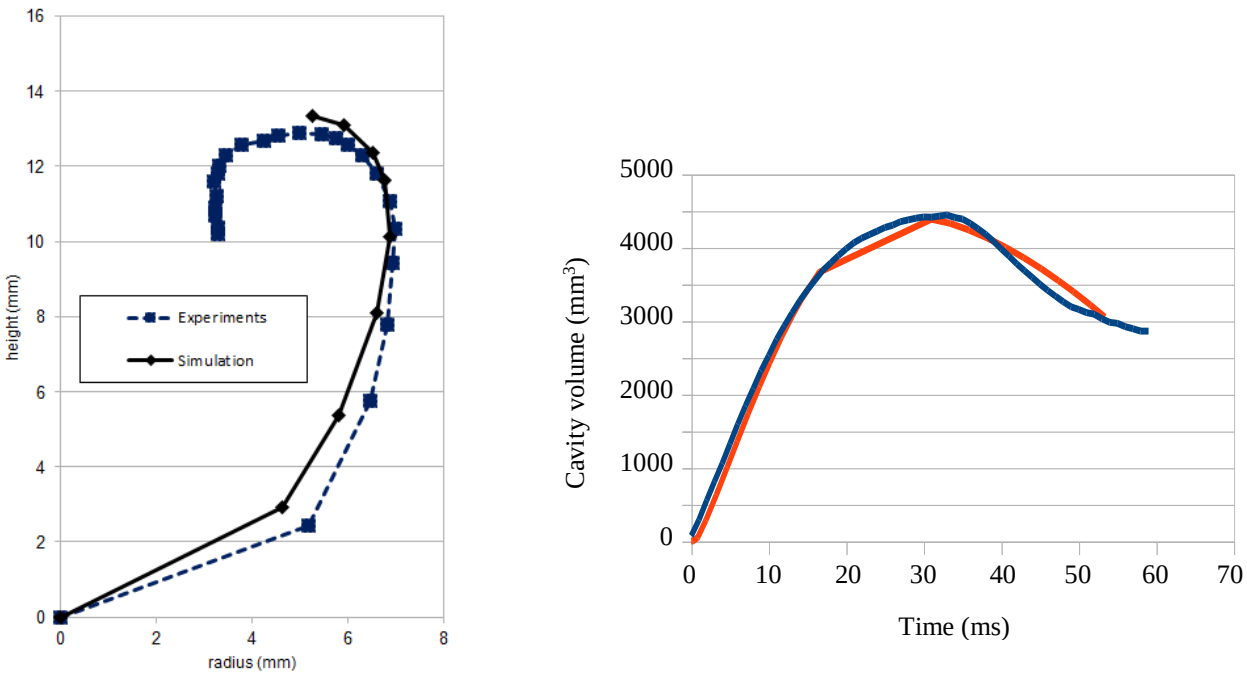

Figure 10: evolutions of (a) the upper rim edge location and (b) cavity volume – experiments in blue and simulations in red

4. CONCLUSION

In the present work, the high energy splash of a water droplet falling on water has been investigated with three dimensional numerical simulations. The calculations have been conducted in the exact same configuration studied previously by Murphy et al. (2015), in order to perform detailed comparisons with the experiments and prepare an in-depth analysis of the splashing mechanisms. The simulations are conducted with the GERRIS open solver, which combines a VOF description of the liquid/gas interfaces and an adaptive octree grid refinement. A post-processing has been developed to reconstruct the various objects created after the drop impact (cavity, crown, ligaments, droplets) and enable their characterization. It was found that 8 levels of refinement applied on an initial domai composed of 8000 cells enable to obtain a reliable qualitative and quantitative agreement with the experiments: all phenomena observed in the high speed videos (crater formation, rise of a thin cylindrical layer of liquid forming a crown that expands outwards and upwards before the upper rim closes at the center, downward liquid jet that pierces the cavity floor) are correctly reproduced at the right times. The cavity volume, the crown radius and height, and the crown edges trajectory also compare very well with the experimental measurements. It shows that the present simulations capture most of the features of the high energy splashing, which will enable to discuss in a future work the physical mechanisms that could not be investigated in the experiments.

.

REFERENCES

[1] A. M. Worthington (1882), On impact with a liquid surface, P. R. Soc. London, **25**:217-230.

[2] Schotland, R. M., 1960: Experimental results relating to the coalescence of water drops with water surfaces. Discuss. Faraday Soc., 30, 72–77, https://doi.org/10.1039/df9603000072.

[3] Engel, O. G., 1966: Crater depth in fluid impacts. J. Appl. Phys., 37, 1798–1808, https://doi.org/10.1063/1.1708605.

[4] Murphy, D. W., C. Li, V. d'Albignac, D. Morra, and J. Katz, 2015: Splash behaviour and oily marine aerosol production by raindrops impacting oil slicks. J. Fluid Mech., 780, 536–477, https://doi.org/10.1017/jfm.2015.431.

[5] Bisighini, A., Cossali, G. E., Tropea, C. & Roisman, I. V. 2010 Crater evolution after the impact of a drop onto a semi-infinite liquid target. Phys. Rev. E 82, 036319.

[6] S. Popinet (2003), Gerris: a tree-based adaptive solver for the incompressible Euler equations in complex geometries, J. of Computational Physics **190**(2):572-600.

[7] R. Scardovelli, S. Zaleski, Analytical relations connecting linear interfaces and volume fractions in rectangular grids, Journal of Computational Physics 164 (1) (2000) 228–237.

[8] S. Popinet, An accurate adaptive solver for surface-tension-driven interfacial flows, J. Comput. Phys. 228 (2009) 5838–5868.

[9] R. DeBar, Fundamentals of the KRAKEN code, Tech. rep., UCID-17366, California Univ., Livermore (USA). Lawrence Livermore Lab. (1974).

[10] E. Aulisa, S. Manservisi, R. Scardovelli, S. Zaleski, Interface reconstruction with least-squares fit and split advection in three-dimensional Cartesian geometry, Journal of Computational Physics 225 (2) (2007) 2301–2319.

[11] M. Francois, S. Cummins, E. Dendy, D. Kothe, J. Sicilian, M. Williams, A balanced-force algorithm for continuous and sharp interfacial surface tension models within a volume tracking framework, Journal of Computational Physics 213 (1) (2006) 141–173.

[12] J. Brackbill, D. B. Kothe, C. Zemach, A continuum method for modeling surface tension, J. Comput. Phys. 100 (1992) 335–354.

[13] H. Samet, Applications of Spatial Data Structures, Addison-Wesley Publishing Company, 1989.

[14] A. M. Khokhlov, Fully threaded tree algorithms for adaptive refinement fluid dynamics simulations, J. Comput. Phys. 143 (2) (1998) 519-543.